GEOPHYSICS, VOL. 85, NO. 5 (JULY-AUGUST 2020); P. B147–B157, 16 FIGS.
10.1190/GEO2019-0490.1

Case History

Sinkhole detection with 3D full seismic waveform tomography

Majid Mirzanejad[1], Khiem T. Tran[1], Michael McVay[1], David Horhota[2], and Scott J. Wasman[1]

ABSTRACT

Sinkhole collapse may result in significant property damage and even loss of life. Early detection of sinkhole attributes (buried voids, raveling zones) is critical to limit the cost of remediation. One of the most promising ways to obtain subsurface imaging is 3D seismic full-waveform inversion. For demonstration, a recently developed 3D Gauss-Newton full-waveform inversion (3D GN-FWI) method is used to detect buried voids, raveling soils, and characterize variable subsurface soil/rock layering. It is based on a finite-difference solution of 3D elastic wave equations and Gauss-Newton optimization. The method is tested first on a data set constructed from the numerical simulation of a challenging synthetic model and subsequently on field data collected from two separate test sites in Florida. For the field tests, receivers and sources are placed in uniform 2D surface grids to acquire the seismic wavefields, which then are inverted to extract the 3D subsurface velocity structures. The inverted synthetic results suggest that the approach is viable for detecting voids and characterizing layering. The field seismic results reveal that the 3D waveform analysis identified a known manmade void (plastic culvert), unknown natural voids, raveling, as well as laterally variable soil/rock layering including rock pinnacles. The results are confirmed later by standard penetration tests, including depth to bedrock, two buried voids, and a raveling soil zone. Our study provides insight into the application of the 3D seismic FWI technique as a powerful tool in detecting shallow voids and other localized subsurface features.

INTRODUCTION

Cover-collapse and cover-subsidence sinkholes are formed due to the spalling, piping, or raveling of the upper sediments (clay, silt, and sands) into cavities or voids within the limestone. They can happen abruptly in a matter of a few hours (cover collapse) or take several years (cover subsidence) to occur and are more prevalent in regions with carbonate or evaporitic rock structures. Sinkhole activities in urban settings can cause significant damage to public infrastructure or private property, even leading to loss of life. With increased cost of development/maintenance, there is a great need for efficient and cost-effective methods to accurately image or identify voids and raveling zones beneath the ground surface.

A variety of noninvasive techniques have been developed to image subsurface features including shallow voids and other anomalies (soft/weak zones or buried objects). The most common techniques are ground-penetrating radar, electrical resistivity tomography, gravity, and seismic methods. The common concept of these methods for identifying voids lies in the contrast of some properties of the void material with its surrounding features. Each method has its own benefits and drawbacks.

Seismic waves and associated waveforms contain material property information of the medium in which they travel. For instance, buried voids can modulate the frequency content, amplitude, and phase of the propagating waveforms, which may be readily used to detect voids. Actual experimentation with test voids within 5 m of

Manuscript received by the Editor 21 July 2019; revised manuscript received 27 April 2020; published online 9 July 2020.
[1]University of Florida, Department of Civil and Coastal Engineering, 365 Weil Hall, P.O. Box 116580, Gainesville, Florida 32611, USA. E-mail: m.mirzanejad@ufl.edu; ttk@ufl.edu (corresponding author); mcm@ce.ufl.edu; scott.wasman@essie.ufl.edu.
[2]Florida Department of Transportation, 5007 N.E. 39th Avenue Gainesville, Florida 32609, USA. E-mail: david.horhota@dot.state.fl.us.

DOI:10.1190/geo2019-0490.1

the ground surface shows that body and surface waveforms are affected by shallow voids (Grandjean and Leparoux, 2004). The detectability of a void depends on many factors, including the source energy and frequency content, material properties, distance between the void and the receivers, and the ratio of void size to the wavelength of the interacting wave.

Seismic wave-based methods, including refraction tomography (Tran and Hiltunen, 2011) and surface wave approaches such as multichannel analysis of surface waves (MASW; Park et al., 1999), also have been used for anomaly/void detection (Cardarelli et al., 2010; Tran and Hiltunen, 2012; Tran and Sperry, 2018). However, these methods only use a small percentage of the information in the waveform to infer subsurface properties, limiting their ability to provide detailed information on voids.

Full-waveform inversion (FWI) methods are the most promising way to obtain true 3D subsurface seismic images for void detection. As documented by Vireux and Operto (2009), the full-waveform approach produces higher resolution models of subsurface structure than approaches that consider only portions of the measured wavefield, such as dispersion curves or first-arrival times. Significant progress on 2D/3D FWI methodologies has been made in the last decade, for various length scales. They vary from meter scales (Romdhane et al., 2011; Bretaudeau et al., 2013; Butzer et al., 2013; Fathi et al., 2016; Nguyen and Tran, 2018; Mirzanejad and Tran, 2019; Tran et al., 2019) to kilometer scales (Ben-Hadj-Ali et al., 2008; Epanomeritakis et al., 2008; Fichtner et al., 2009; Plessix, 2009; Tape et al., 2010; Vigh et al., 2011; Warner et al., 2013; Ha et al., 2014; Métivier et al., 2016; Shen et al., 2018).

For the sinkhole application, Tran et al. (2013) show that the 2D FWI approach could successfully detect buried voids as well as characterize variable soil/rock layering. However, the 2D approach requires that the test lines be placed directly over the voids. If test lines are off center of the voids, they will be distorted and shifted, or even invisible, depending on the distance between the test lines and the voids. Additionally, the 2D approach does not correctly account for point source modeling and out-of-plane scattering effects. The latter effects generally require the application of phase and amplitude correction factors. The use of a 3D FWI approach could eliminate the need for these corrections as well as detect off-line voids and horizontal variability. In summary, 3D FWI has the potential of providing a high-resolution 3D image of the subsurface structure.

Recently, a 3D Gauss-Newton full-waveform inversion method (3D GN-FWI) has been developed (Tran et al., 2019) based on an elastic finite-difference forward model to generate a synthetic wavefield and a Gauss-Newton approach to minimize the misfit function to extract a 3D grid of material properties. Gauss-Newton inversion is well recognized as a robust and effective technique for numerical optimizations of nonlinear problems, with faster convergence rates than a traditional gradient method (Pratt et al., 1998; Sheen et al., 2006; Papadimitriou and Giannakoglou, 2008). More importantly, the inverse Hessian matrix used in the Gauss-Newton inversion acts as a weighting function to balance the gradient vector and model updating during the inversion. It reduces the dominancy of Rayleigh waves (lower weights for shallow cells) and increases the contribution of body waves in the far-field data (greater weights for deeper cells), and thus helps resolve deeper structures. The 3D GN-FWI method has successfully characterized in situ soil/rock layering including the existence of soft soil zones. Compared to results of the same field data analyzed by a cross-adjoint 3D FWI (Nguyen and Tran, 2018), shear-wave (S-wave) velocity (V_S) profiles from the 3D GN-FWI are more consistent with the standard penetration test (SPT) N-values (Tran et al., 2019).

In this study, we investigate the capability of the 3D GN-FWI method in detection of anomalies (e.g., voids, layering, as well as horizontal variability — pinnacles, ravel zones). First, the method is tested on a synthetic data set obtained from a challenging synthetic model with two embedded voids and variable soil/rock layers. Then, it is tested at a site at the University of Florida main campus, which contains a buried plastic culvert. The goal is to determine if the method could accurately detect and characterize the known cavity and to verify its validity on noisy field data (versus noise-free synthetic data). Finally, the method is tested on field data acquired at a retention pond in Newberry, Florida, in a blind study where no previous knowledge of voids and soil/rock layering existed. The seismic results are confirmed with SPT field verification. Data acquisition, analysis, visualization of subsurface features, and field verification of the detected voids are elaborated in the following sections.

METHODOLOGY AND IMPLEMENTATION

The 3D GN-FWI method used in this study is reported in detail by Tran et al. (2019). Forward simulation uses a 3D elastic wave propagation described by the following stress equilibrium and constitutive equations:

$$\rho \frac{\partial v_i}{\partial t} = \frac{\partial \sigma_{ij}}{\partial x_j} + \mathrm{f_i}, \tag{1}$$

$$\frac{\partial \sigma_{ij}}{\partial t} = \left(\lambda \frac{\partial v_k}{\partial x_k} + 2\mu \frac{\partial v_i}{\partial x_j}\right)\delta_{ij} + \mu\left(\frac{\partial v_i}{\partial x_j} + \frac{\partial v_j}{\partial x_i}\right)(1 - \delta_{ij}). \tag{2}$$

In the above set of equations, σ_{ij} is the ijth component of stress tensor (i, $j = 1, 2, 3$), v_i is the particle velocity, $\mathrm{f_i}$ is the external body force, ρ is the mass density, δ_{ij} is the Kronecker delta function, and λ and μ are Lamé's coefficients of the material. Repetition of a subscript (e.g., k, k) denotes summing over the indices ($k = 1, 2, 3$).

The classic velocity-stress staggered-grid finite-difference method (Virieux, 1986) is used to solve the wave equations with second-order accuracy in time and space. The image technique (Robertsson, 1996) is used to simulate a free-surface boundary condition at the ground surface (top), and the perfectly matched layer (Komatitsch and Martin, 2007) is used at four vertical and bottom boundaries to absorb the outgoing waves to eliminate spurious reflection back into the model space being analyzed. See Nguyen and Tran (2018) for more details on the forward simulation.

The Gauss-Newton optimization technique is used iteratively to minimize the error between the simulated data and the measured field data to extract individual cell material properties. The error is defined as

$$\mathrm{E}(\mathbf{m}) = \frac{1}{2}\|\mathrm{F}(\mathbf{m}) - \mathrm{d}\|^2, \tag{3}$$

where $\mathbf{F}(\mathbf{m})$ denotes the simulated data (all shots and receivers) associated with model $\mathbf{m}$, which is obtained through the solution of

equations 1 and 2. Model $\mathbf{m}$ is composed of the V_S and V_P of the cells within the domain and is stored in a column vector. Similarly, $\mathbf{d}$ denotes the observed data gathered from the field experiment using a 2D layout of shots and receivers.

To minimize the error, model $\mathbf{m}$ is updated iteratively as

$$\mathbf{m}^{n+1} = \mathbf{m}^n - \alpha^n[\mathbf{J}^t\mathbf{J} + \lambda_1\mathbf{P}^t\mathbf{P} + \lambda_2\mathbf{I}^t\mathbf{I}]^{-1}\mathbf{J}^t\Delta\mathbf{d}, \quad (4)$$

where $\mathbf{J}$ is the Jacobian matrix, which denotes the partial derivative of the wavefield with respect to each model parameter (V_S and V_P in the cells). Symbol $\mathbf{I}$ stands for the identity matrix, and matrix $\mathbf{P}$ is determined via a 3D Laplacian operator with its elements of either 1, −6, or 0. Parameter α^n denotes the step length, which is fixed at 0.5 for the entire analysis. Parameters λ_1 and λ_2 are used to improve the invertibility of the approximate Hessian matrix ($\mathbf{H_a} = \mathbf{J^tJ}$) and regularization. Values λ_1 and λ_2 can range from zero to infinity, with larger values leading to greater optimization stability but resulting in smoother inverted models. Using trial runs, coefficients λ_1 and λ_2 are found as 0.02 and 0.0005 times of the maximum value of H_a, respectively, to give a good compromise and are used in the study for void detection.

For the efficient calculation of the Jacobian matrix, an implicit method is developed by Tran et al. (2019) as

$$\mathbf{J}^p_{s,r} = \boldsymbol{F}_x * \boldsymbol{R}_x + \boldsymbol{F}_y * \boldsymbol{R}_y + \boldsymbol{F}_z * \boldsymbol{R}_z, \quad (5)$$

where $\boldsymbol{F}_x$, $\boldsymbol{F}_y$, and $\boldsymbol{F}_z$ are the virtual sources calculated from the forward wavefields that are generated by a source at the sth shot location and recorded at the location of model parameter m_p in the x, y, and z directions, respectively (see equations 9–14 of Tran et al., 2019 for the governing wave equations). The variables $\boldsymbol{R}_x$, $\boldsymbol{R}_y$, and $\boldsymbol{R}_z$ are the backward wavefields generated by a source at the rth receiver location and recorded at the model parameter m_p location in the x, y, and z directions, respectively. The symbol * denotes the convolution operator. Using equation 5, only $(NS + NR)$ forward simulations are required to calculate $\mathbf{J}$.

APPLICATIONS

Synthetic model

Synthetic experimentation or testing is a cost-effective approach to evaluate the merits of the 3D GN-FWI method for void detection. It starts with an assumed model, the so-called true model, which represents an in situ field condition. This true model then is fed into the forward simulation, and the response (i.e., synthetic data) is recorded and assumed to represent the field data. The data then are used in the 3D GN-FWI algorithm, and the inverted result is compared to the true model for assessment of the algorithm.

For the synthetic experiment, a 2D array of 72 receivers and 91 sources (shots) with a spacing of 3 m, covering an area of 36×18 m^2 is defined (Figure 1). The receiver and source grids are 6×12 and 7×13 patches, respectively, both at 3 m spacing. The entire model of $36 \times 18 \times 18$ m^3 (length × width × depth) is discretized into 30,625 grid points with a grid spacing of 0.75 m. The choice of grid spacing is based on a balance of numerical stability and processing time, as well as the availability of computational resources to facilitate source and receiver placement on the numerical grid. The true model shown in Figure 2a is representative of typical karst features in Florida having a low-velocity layer ($V_S = 300$ m/s and $V_P = 600$ m/s) of sandy/silty soil overlying a high-velocity layer ($V_S = 700$ m/s and $V_P = 1400$ m/s) of weathered limestone. The varying interface separates the two layers with pinnacles and valleys that represent the chemical and physical weathering of the karst feature. The model contains two embedded voids of 3 and 4.5 m in size, placed at 6 and 12 m below the ground surface

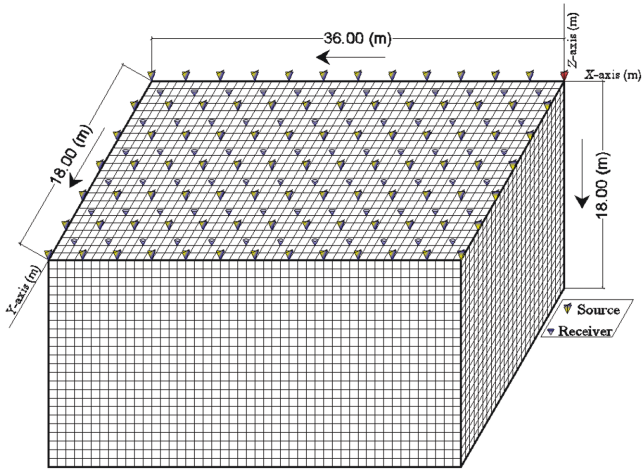

Figure 1. Synthetic and Newberry field experiments: true-to-scale meshing and test configuration. (The source shown in red denotes the sample shot used in Figure 4.)

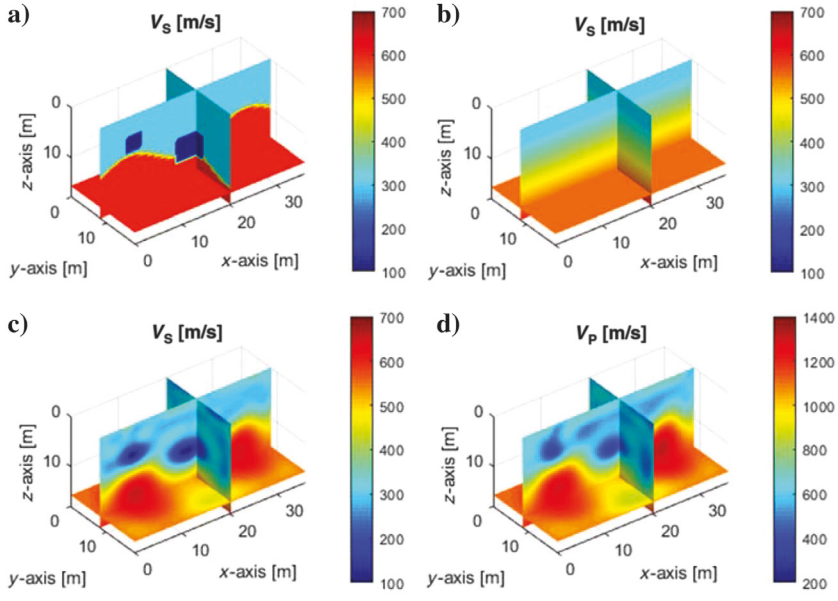

Figure 2. Synthetic experiment: (a) distribution of V_S (m/s) for the true model ($V_P = 2V_S$, except V_P of voids as 300 m/s), (b) distribution of V_S (m/s) for the initial model used at the beginning of inversion ($V_P = 2V_S$), and (c and d) distribution of V_S (m/s) and V_P (m/s) for the final inverted model at 5–35 Hz analysis.

($z = 0$ m), respectively. The simulated air-filled voids have V_S of 0 m/s and V_P of 300 m/s.

The forward simulation is conducted on the true model (Figure 2a) for each of the 91 shots separately. A Ricker wavelet with the central frequency of 15 Hz is used to represent the source signature. The simulated wavefield is recorded for all 72 receivers and 91 shots and is used for the FWI analysis as experimental field data. Source and receiver are vertical and located on the free surface. The source is induced as a vertical force (f_i) in equation 1, which is similar to an impact load used in the field experiment.

Two inversion runs are conducted at frequency bandwidths of 5–25 Hz and 5–35 Hz. Analysis begins with the first filtered at 5–25 Hz wavefield using the basic initial model (Figure 2b). The initial model is a 1D profile with V_S linearly increasing from 300 m/s at the ground surface to 600 m/s at a depth of 18 m with $V_P = 2V_S$. Such an initial model can be established via spectral analysis of the wavefield as detailed in the field data applications. The first inversion is run for the maximum number of preset iterations (20 iterations), and the data-domain residuals are reduced consistently from the normalized value of 1.0 at the beginning of the inversion to less than 0.1 at the end of iteration 20 in the first run (Figure 3).

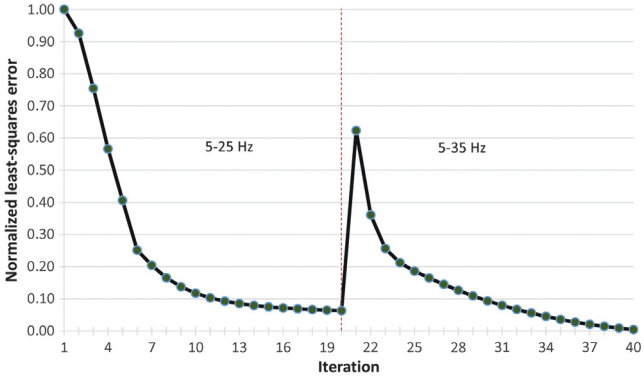

Figure 3. Synthetic experiment: normalized least-squares error for the entire inversion run (iterations 1–40).

Next, the 5–35 Hz bandwidth filtered experimental data are used in the second inversion run with the results from the first run as the input model. The second inversion is run for an additional 20 iterations, with the normalized error consistently decreasing to a value of 0.01 at the end of iteration 40 (Figure 3). Note that the increase in the normalized error at the start of the second run is caused by the sudden introduction of the higher frequency data, while the model has not yet adjusted for wave propagation of the higher frequency data (shorter wavelength).

Figure 4 shows the waveform comparison for a sample shot between the observed data from the true model and the estimated data from the initial model (iteration 1) and the final inverted model (iteration 40). The good match of the first-arrival signals on the observed and estimated waveforms at iteration 1 (Figure 4a) indicates the suitability of the initial model (Figure 2b) used for this experiment. The waveform match improves during the analyses, and the observed and estimated data are almost identical at the end of 40 iterations (Figure 4b). This suggests that the 3D GN-FWI code successfully approached a global solution, matching the phase and amplitudes throughout the inversion process. It is noted that the perfect fit of the data at the end of 40 iterations can be achieved only when inverting noise-free self-generated synthetic data, and this is not expected for noise-corrupted field data.

Figure 2c and 2d presents the final inverted result of the second run (iteration 40) for the V_S and V_P profiles, respectively. The existence of the two embedded voids is confirmed, and their locations, depths, and overall sizes are well characterized. Soil layering and the variable layer interface topography also are successfully recovered. The V_S and V_P of voids are generally recovered, but the inverted values of approximately 100 m/s for V_S and 350 m/s for V_P are higher than their true values. This is due to the regularization used in inversion that constrains adjacent cells and creates a smooth model.

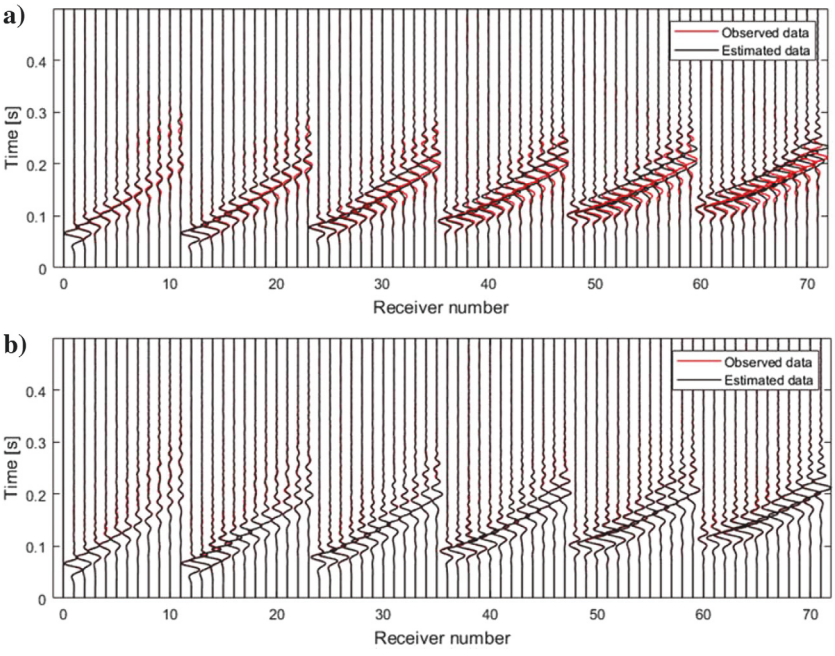

Figure 4. Synthetic experiment: waveform comparison for a sample shot (shown in red in Figure 1) between the observed data and estimated data associated with (a) the initial model and (b) the final inverted model.

Figure 5a, 5b, and 5c presents the 3D rendering of the true V_S and final models for V_S and V_P, respectively. The two voids and the variable layer interface are successfully recovered and imaged. Results from this synthetic experiment show the great potential of the 3D GN-FWI in imaging subsurface anomalies.

Buried culvert detection

After the successful detection of the synthetic voids, the 3D GN-FWI method is tested at a site with a buried plastic culvert on the campus of the University of Florida. The culvert is a high-density polyethylene corrugated pipe of 1 m diameter, embedded approximately 3 m beneath

DOI:10.1190/geo2019-0490.1

the ground surface. Due to limited space for seismic testing, the culvert diagonally spans across the test area (Figure 6a). A 2D array of 72 receivers (4.5 Hz vertical geophones) and 91 sources (shots) are used on the ground surface (Figure 6b), covering a test area of 18×9 m^2. The receiver and source grids are 6×12 and 7×13, respectively, both at 1.5 m spacing. A sledgehammer is used to induce seismic waves at each of the 91 shot locations, and the wavefield generated from each shot is recorded simultaneously by the 72 geophones.

The spectral analysis of measured culvert data for one row of 12 geophones is shown in Figure 7, where the phase velocity is almost constant at 180 m/s for a wide frequency range (10–60 Hz). Based on the spectral analysis, an initial homogeneous model of V_S equal to 180 m/s is chosen with $V_P = 2V_S$. A homogeneous mass density of 1800 kg/m^3 is assumed and kept constant for the entire inversion. The medium depth is selected as 9 m, or one half of the larger test dimension, to maintain a good signal coverage in the analyzed domain. We note that one can select a larger medium depth, but the model update at the deeper structure during inversion is small due to limited signal passing through.

The entire inversion process is performed with a single run on the collected field data at the frequency bandwidth of 10–60 Hz with a central frequency of 45 Hz. This wide range of frequency is selected because the initial model could predict the true data well for the entire frequency range and it was not necessary to conduct analyses at separate frequency ranges. An $18 \times 9 \times 9$ m^3 (length $\times$ width $\times$ depth) numerical grid with grid spacing of 0.375 m is used during forward simulation and model updating (Figure 6b). The grid spacing of 0.375 m is selected as a quarter of the shot/receiver spacing (1.5 m) to conveniently assign the shot/receiver locations to the numerical nodes.

During inversion, source signatures are estimated for individual source locations as detailed in Tran and Luke (2017) and used for wave simulation. In the time domain, the wavefield is a convolution of the source signature and the Green's function. In the frequency domain, it is equivalent to a multiplication as $\mathbf{F}(f, \mathbf{x}, \mathbf{m}) = \mathbf{G}(f, \mathbf{x}, \mathbf{m}) \cdot \mathbf{W}(f)$, where $\mathbf{F}$, $\mathbf{G}$, and $\mathbf{W}$ are the wavefield, the Green's function, and the source associated with a frequency f, respectively; $\mathbf{m}$ is a model describing material properties (V_S, V_P); and $\mathbf{x}$ is the source and receiver coordinates. With a given model $\mathbf{m}$, the Green's function can be calculated by the forward simulation (solution of equations 1 and 2) with an assumed source $\mathbf{W}(f)$ (Ricker wavelet with central frequency of 45 Hz) as $\mathbf{G}(f, \mathbf{x}, \mathbf{m}) = \mathbf{F}(f, \mathbf{x}, \mathbf{m})/\mathbf{W}(f)$. The estimated source then is obtained from measured field data $\mathbf{d}(f, \mathbf{x})$ and the Green's function as $\mathbf{W}_{\text{est}}(f) = \mathbf{d}(f, \mathbf{x})/\mathbf{G}(f, \mathbf{x}, \mathbf{m})$. Because the measured data include multiple source-receiver offsets, the best-fit source wavelet $\mathbf{W}_{\text{est}}(f)$ for each frequency f is obtained by applying a least-squares technique to solve the overdetermined system of equations (Ernst et al., 2007). The inverse Fourier transform is used to convert the estimated source from the frequency domain to the time domain. The estimated source then is applied as a vertical force (f_i) in equation 1 for wave simulation.

To account for the offset-dependent amplitude attenuation caused by intrinsic attenuation effects inherent in the observed field data, the estimated data are adjusted by a correction factor of the form $y(r) = Ar^{\alpha}$, with the source-receiver distance denoted by r. Factor A and exponent α are determined in an iterative least-squares

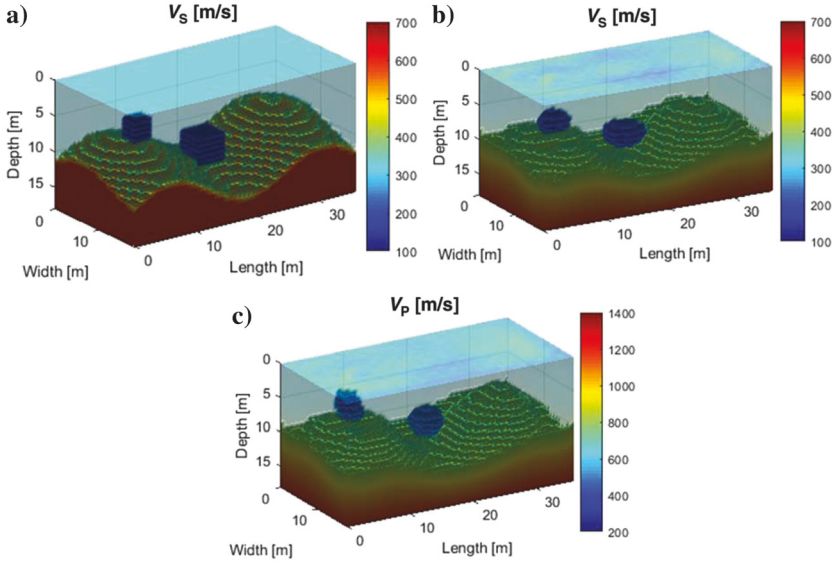

Figure 5. Synthetic experiment: (a) 3D rendering of the true model, and (b and c) the final inverted result for V_S (m/s) and V_P (m/s).

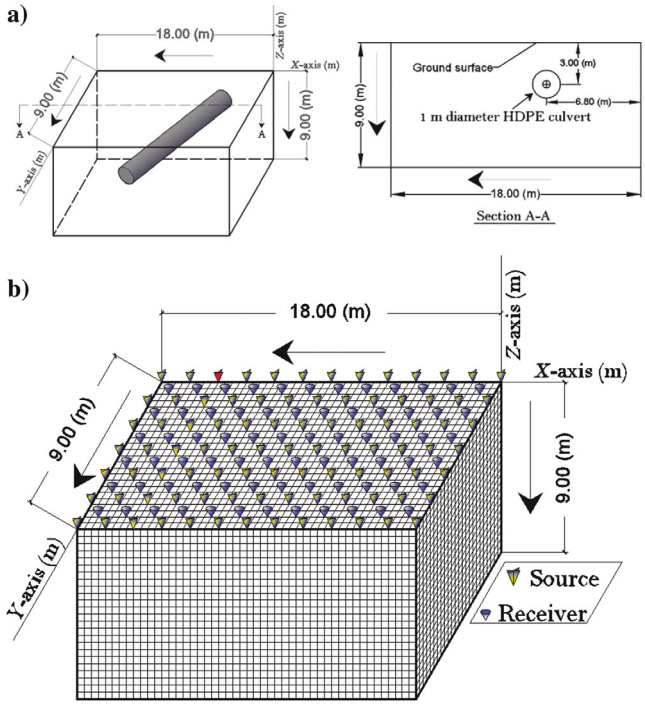

Figure 6. Field experiment on the culvert: (a) 3D depiction of culvert location with respect to the test site (left) and vertical view of the pipe at $y = 4$ m (right), and (b) true-to-scale meshing and test configuration. (The source shown in red denotes the sample shot used in Figure 9.)

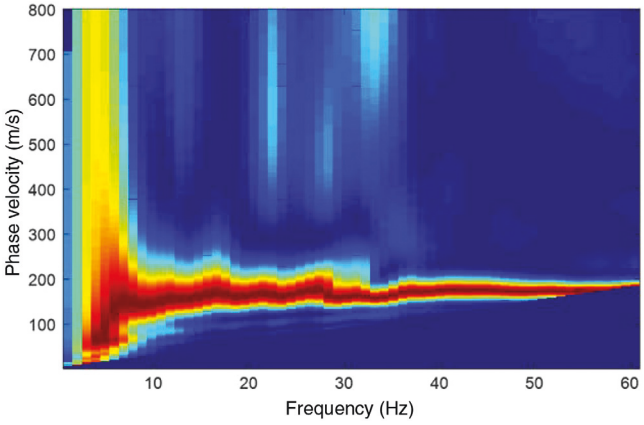

Figure 7. Field experiment on the culvert: dispersion curve of the measured data for one sample shot and one line of 12 geophones.

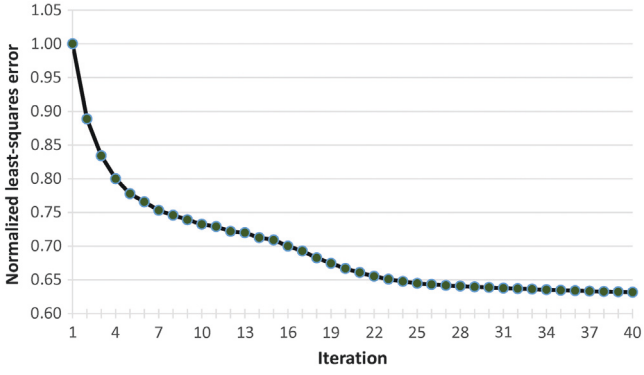

Figure 8. Field experiment on the culvert: normalized least-squares error for the entire inversion analysis (iterations 1–40) on data at the frequency bandwidth of 10–60 Hz.

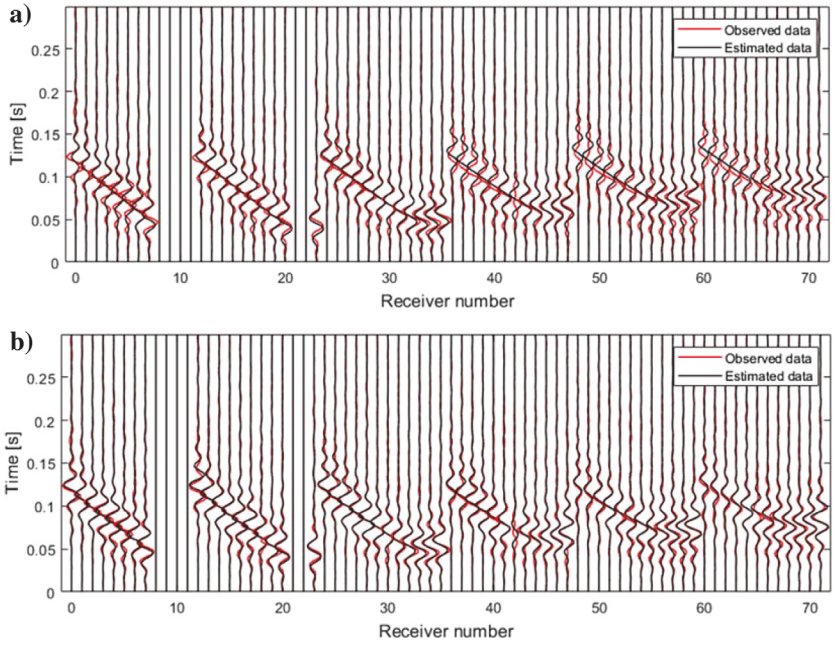

Figure 9. Field experiment on the culvert: waveform comparison between the observed data and the estimated data associated with (a) the initial model and (b) the final inverted model for a sample shot (shown in red in Figure 6).

inversion process by minimizing the energy of the waveform residuals. The values of A and α are determined at the beginning of the inversion run and are kept constant for the entire inversion analysis. The correction factor of $y(r)$ only corrects for amplitude changes as a result of material anelasticity and does not account for changes in phase or material dispersion. Unlike the 2D approach, the 3D forward simulation inherently accounts for geometric spreading and point source effects in the data.

The inversion analysis is stopped when it reaches the preset maximum number of iterations (40 iterations), which takes approximately 15 hours on a desktop computer (32 cores of 3.46 GHz each and 256 GB of memory). As shown in Figure 8, the least-squares error consistently decreases during the inversion process from the normalized value of 1.0 at the beginning to 0.63 at the last iteration. Figure 9 shows the waveform comparison of a sample shot between the measured (observed) data from the field experiment and the estimated data associated with the initial model (iteration 1) and the final inverted model (iteration 40). The waveform match improves for all 72 channels during the inversion. No cycle skipping or matching of wrong peaks is observed, suggesting the sufficiency of the homogeneous initial model.

Figure 10 shows the inverted V_S profile, with 3D perspective views of a horizontal cut at depth $z = 3$ m (Figure 10a) and a vertical cut at the distance $y = 4.5$ m (Figure 10b). The 3D FWI method successfully identifies the existence of the culvert, well characterized its depth and direction, and generally recovers its diameter. The rendering of the result (Figure 10c and 10d) clearly shows the position, direction, and depth of the culvert in the 3D domain. The inverted V_P profile is very similar to V_S; thus, it is not included herein.

Newberry sinkhole detection

Next, the 3D GN-FWI method is applied to data sets gathered at a retention pond in Newberry, Florida, for detection of unknown voids. The test site consists of medium-dense, fine sand and silt underlain by highly variable limestone. The test area is divided into two adjoining zones 1 and 2, each covering an area of $18 \times 36\,\mathrm{m}^2$ (Figure 11a). This is a blind seismic survey (class-A prediction) because the test area is an open and flat area of ground with no indication of subsidence or chimneys. More importantly, no previous knowledge of voids, soil/rock layering, pinnacles, or raveling exists at the test area. Because no anomalies are detected in test zone 2, only data obtained from test zone 1 are presented in this paper.

Like the experiment on the synthetic model, the seismic field experiment is conducted with a test configuration of 72 receivers (4.5 Hz vertical geophones) and 91 shots (source impacts) located in 2D uniform grids on the ground surface (Figure 1). The receiver and source grids are 6×12 and 7×13, respectively, both at 3 m spacing. A propelled energy generator (PEG) with a 40 kg drop-weight (Figure 11b) is used to induce seismic waves at each of the 91 shot locations (Figure 1), and the wavefield generated from each shot is recorded simultaneously by the 72 geophones.

DOI:10.1190/geo2019-0490.1

A 1D initial model with depth is developed via spectral analysis of the measured wavefields for a sample shot using one line of 12 geophones (Figure 12). The analysis reveals that the phase velocities are from 250 to 600 m/s at the frequency range of 7–35 Hz. The V_S near the ground surface associated with the higher frequencies is known to be approximately 250 m/s, and the average V_S of the half-space is approximately 600 m/s. Similar to the synthetic case, the initial model (Figure 13a) is established having V_S increasing with depth from 250 m/s at the surface to 600 m/s (the V_S of the half-space) at the bottom of the model. Again, the model depth of 18 m is taken as one half of the longer dimension of the test area to maintain good signal coverage in the analyzed domain. The V_P value is calculated from V_S and a constant Poisson's ratio of 1/3 for the entire medium, which is based on the characteristic range (1/4 to 1/2) for general soil/rock. It should be noted that no prior information of any subsurface features is needed for the initial model.

A fixed mass density of 1800 kg/m^3 is assumed for the soil and limestone for the entire domain. Because of dominant Rayleigh waves in measured surface-based waveform data that are not very sensitive to mass density, our efforts to invert the mass density have been shown to be unsuccessful. Also, keeping a constant mass density during inversion does not have any major effects on the accuracy of our inverted V_S and V_P, which again can be the result of the insensitivity of the dominant Rayleigh waves to mass density variations. There is also evidence from another study (Operto et al., 2013) that keeping density constant does not affect successful inversion of velocity using FWI.

The analysis consists of a $36 \times 18 \times 18$ m^3 (length × width × depth) numerical grid with grid spacing of 0.75 m for the forward simulation and model updating (Figure 1). A grid spacing of 0.75 m is selected as a quarter of the shot/receiver spacing. The measured data are filtered through two frequency bandwidths: 5–25 Hz and 5–35 Hz prior to their input to the FWI analyses. Like the case of the buried culvert, the source signature is estimated by deconvolution of the measured data with the Green's function for each shot and is used as a vertical force (f_i in equation 1) for wave simulation. Similarly, the estimated data generated by the forward simulation are corrected $[y(r) = Ar^{\alpha}]$ for amplitude attenuation effects by applying an offset-dependent correction factor for each iteration.

Like the synthetic model analysis, two inversion runs are performed. The first run uses the initial model (Figure 13a) with the frequency range 5–25 Hz data. The inversion profiles from the first run then are used as the input model for the second analysis using the frequency range 5–35 Hz data. Both inversions are stopped after 20 iterations, the preset maximum number of iterations, after taking approximately 40 hours on the same computer used for the culvert analysis. The FWI algorithm consistently

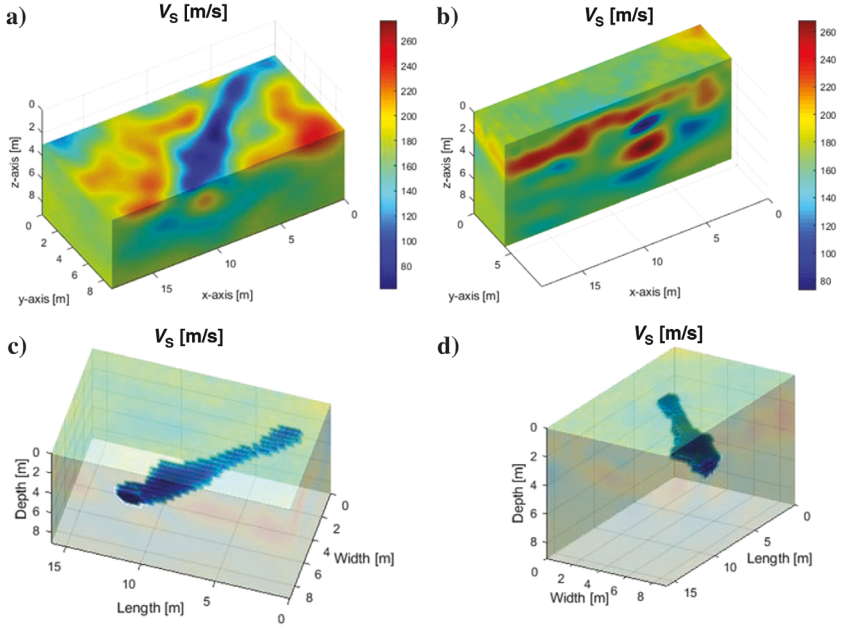

Figure 10. Field experiment on the culvert: (a and b) perspective view of the inverted result, and (c and d) 3D rendering of the result at two angle views.

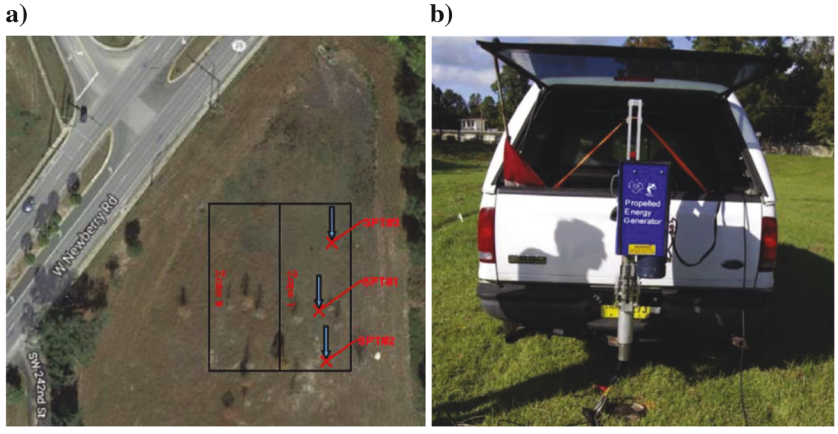

Figure 11. Newberry test site: (a) location of the test zones and SPT tests and (b) 40 kg PEG used to generate seismic waves.

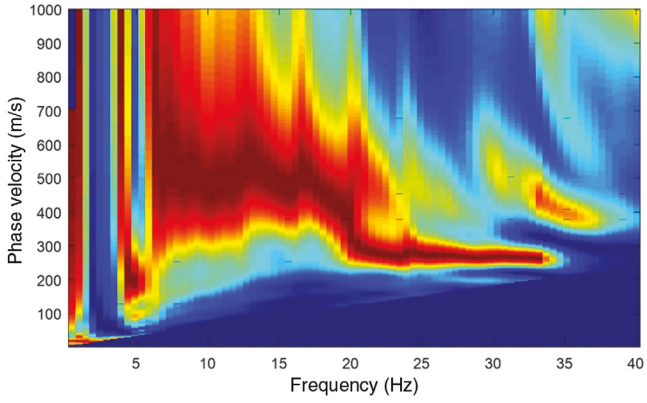

Figure 12. Field experiment of the Newberry site: dispersion curve of measured data for one sample shot and one line of 12 geophones.

DOI:10.1190/geo2019-0490.1

improves on the initial model, as well as decreases the normalized error to approximately 50% of the initial error by the end of the 5–35 Hz frequency analysis (Figure 14).

Shown in Figure 15 is the waveform comparison for a sample shot between the observed data from the field experiment, the initial model (iteration 1), and the final inverted model (iteration 40). Evidently, the waveform match improves significantly during the inversion analyses. The observed and the final estimated data are well matched (Figure 15b), suggesting the sufficiency of the initial model and the ability of the FWI method to find the optimum solution to the nonlinear inversion problem.

The final inverted result on 5–35 Hz data is shown in Figure 13b for V_S and Figure 13c for V_P. The V_S profile (Figure 13b) consists of a softer layer ($V_S \sim 150 - 300$ m/s), underlain by a stiffer layer ($V_S \sim 400 - 700$ m/s). There are three low-velocity zones at the left, middle, and right of the medium. The V_P profile (Figure 13c) is consistent with the V_S profile, including the softer and stiffer layers, and the three low-velocity anomalies. Based on soil types from the SPT samples, the softer and stiffer layers are fine sand with silt and weathered limestone, respectively. There is an indication of high-velocity zones close to the ground surface (top 3 m) for V_P and V_S. These primarily are associated with locally compacted materials due to testing vehicles and isolated weathered limestone. They also could be inversion artifacts near the source/receiver locations.

For better viewing of subsurface features, Figure 16 presents a 3D rendering of the final inverted V_S and V_P profiles. In the V_S image, cells with $V_S < 100$ m/s (low-velocity anomalies) or $V_S > 400$ m/s (limestone) are shown, whereas cells with 100 m/s $< V_S < 400$ m/s are made to be transparent. Similarly, cells with $V_P < 400$ m/s (low-velocity anomalies) and $V_P > 800$ m/s (limestone) are shown in the V_P image. Three low-velocity anomalies and variable limestone surfaces are displayed clearly in the V_S and V_P images.

For verification of the seismic results, SPTs are conducted at the three anomaly locations (Figure 11a). All three SPTs are terminated at the top of the limestone bedrock. Shown in Figure 16b are the locations, depths, and N-values of each SPT. The existence of two voids at the locations marked by SPT#1 and SPT#3 is confirmed by the lack of soil/rock material in the sampler, as well as the drop of the rod due to its weight (N-value of 0). The void at SPT#1 is from 4 to 7 m depth, and the void at SPT#3 is smaller, from 4 to 5 m depth. The SPT#2 has a range of low N-values (2–6), suggesting a raveling zone of very soft material. However, no void is encountered at this location. The top of the bedrock at 6–7 m depths identified by seismic testing at $V_S \sim 500$ m/s also agrees with the SPT results.

Lastly, crosstalk can have a negative impact on the accuracy of FWI results. For sinkhole detection, the V_S and V_P of low-velocity anomalies often are correlated in space (low values at same locations), and crosstalk is not a critical issue. More importantly, the Hessian in the Gauss-Newton method helps suppress the crosstalk between inverted parameters (Pan et al., 2016); thus, the V_S and V_P of the anomalies can be inverted independently. The inverted $V_S <$ 100 m/s and $V_P < 400$ m/s for air-filled voids at the Newberry site clearly show the accuracy of the presented method.

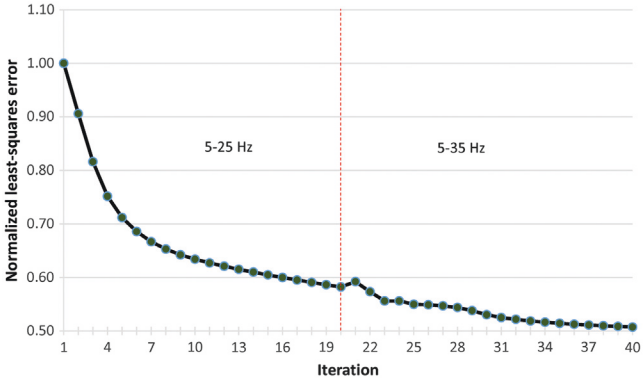

Figure 14. Field experiment of the Newberry site: normalized least-squares error for the entire inversion analysis (iterations 1–40).

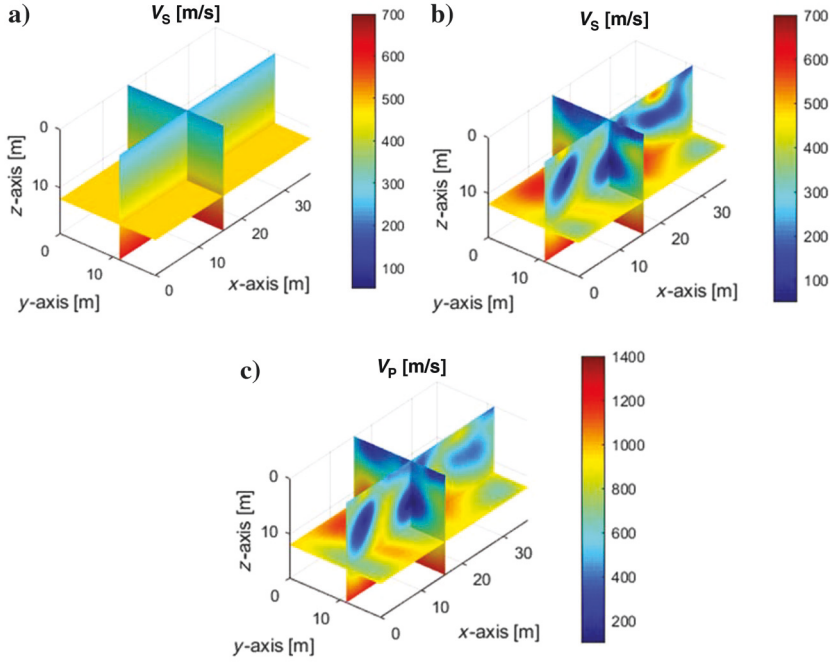

Figure 13. Field experiment of the Newberry site: (a) distribution of V_S (m/s) for the initial model used at the beginning of the inversion ($V_P = 2V_S$), and (b and c) distribution of V_S (m/s) and V_P (m/s) for the final inverted model at 5–35 Hz.

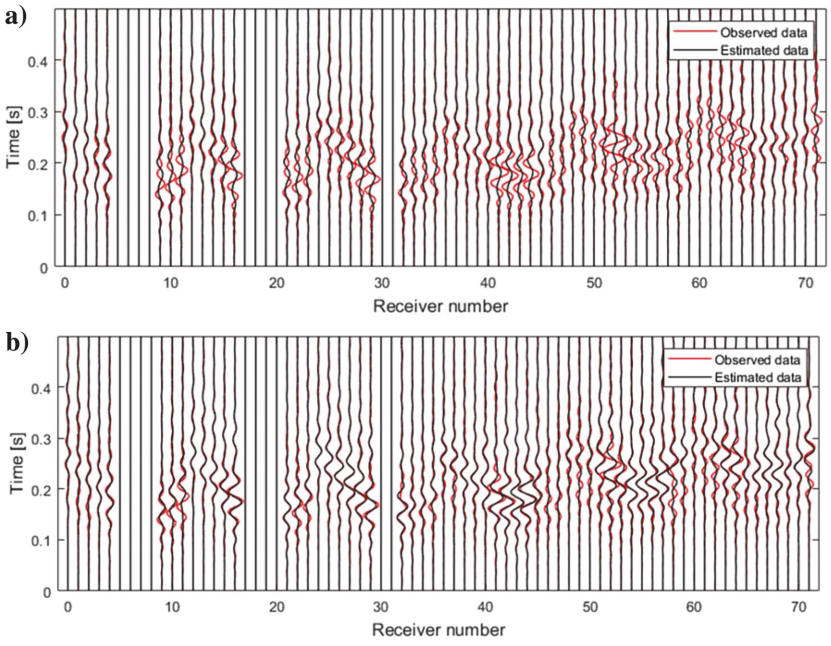

Figure 15. Field experiment of the Newberry site: waveform comparison for a sample shot associated with (a) the initial mode and (b) the final inverted model. Poor channels are removed from the waveform analyses.

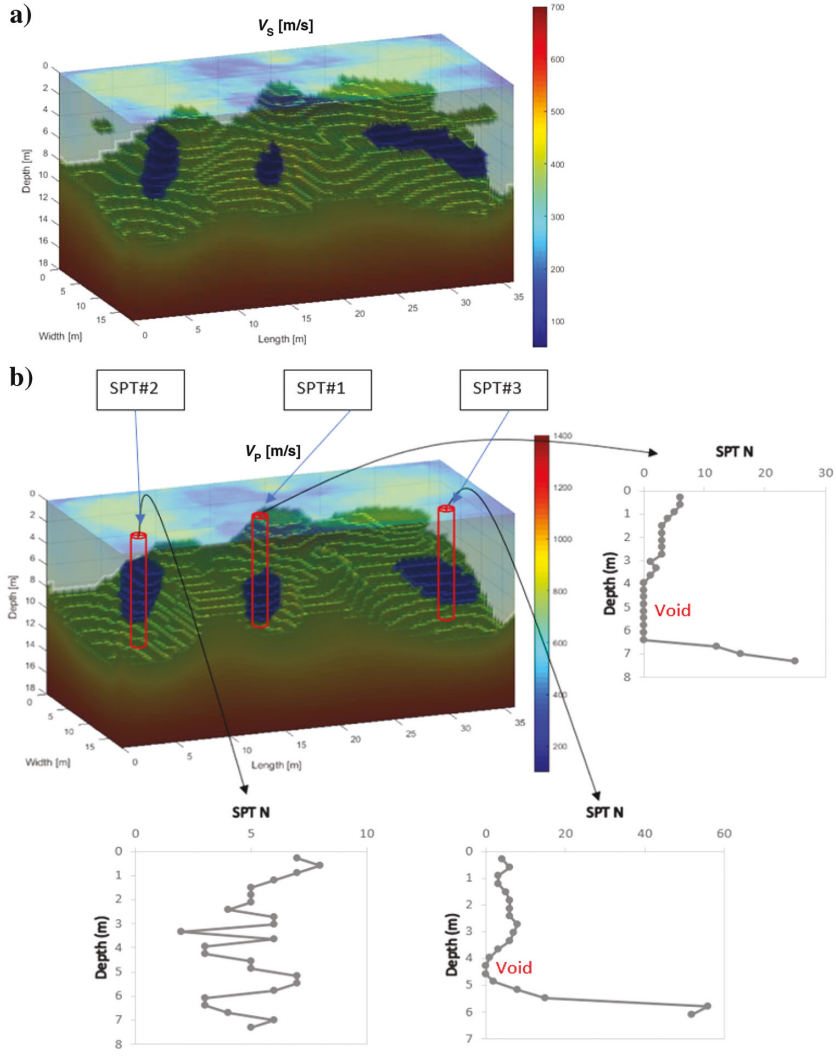

Figure 16. Field experiment of the Newberry site: (a) 3D rendering of the inverted V_S and (b) 3D rendering of the inverted V_P together with the SPT locations, depths, and N-values. Two voids are confirmed at SPT#1 and SPT#3, and soft soil (raveling) zone at SPT#2.

DOI:10.1190/geo2019-0490.1

DOI:10.1190/geo2019-0490.1

CONCLUSION

This paper reports the first-time application of a 3D GN-FWI algorithm for detection of sinkhole attributes (buried voids, raveling zones). The method is based on a finite-difference solution of 3D elastic wave equations and the Gauss-Newton optimization. Full-scale synthetic and field experiments are conducted to assess the ability of the method in detecting subsurface 3D anomalies, as well as characterizing variable 3D soil/rock layering. The method is tested first on a challenging synthetic model with a variable soil layer interface and two embedded voids. Then, it is evaluated on the data sets gathered at the University of Florida campus with a known buried culvert and a Newberry site with unknown site subsurface soil/rock information. The results of the synthetic analysis indicate that the method could accurately detect the existence of two separate embedded voids with variable soil/rock layering present. Testing on the underground culvert shows that the method identifies the existence, direction, as well as depth of the culvert, and the culvert diameter generally is characterized over its length. In the case of the unknown Newberry site, the 3D GN-FWI method shows excellent capabilities in identifying the layering and horizontal variability (rock surfaces, pinnacles) as well as multiple voids and low-velocity anomalies (e.g., raveling zones). The Newberry seismic results are confirmed by invasive SPT sampling (soil versus rock), loss of circulation, rod drop (voids), and low variable N-values (ravel zone).

ACKNOWLEDGMENTS

This study was supported by the National Science Foundation: grants CMMI-1637557, CMMI 1850696, and the Florida Department of Transportation (FDOT): grant BDV31-977-82. We thank the FDOT for conducting the SPT data.

DATA AND MATERIALS AVAILABILITY

Data associated with this research are available and can be obtained by contacting the corresponding author.

REFERENCES

Ben-Hadj-Ali, H., S. Operto, and J. Virieux, 2008, Velocity model building by 3D frequency-domain, full-waveform inversion of wide-aperture seismic data: Geophysics, **73**, no. 5, VE101–VE117, doi: 10.1190/1.2957948.

Bretaudeau, F., R. Brossier, D. Leparoux, O. Abraham, and J. Virieux, 2013, 2D elastic full-waveform imaging of the near-surface: Application to synthetic and physical modelling data sets: Near Surface Geophysics, **11**, 307–316, doi: 10.3997/1873-0604.2012067.

Butzer, S., A. Kurzmann, and T. Bohlen, 2013, 3D elastic full-waveform inversion of small-scale heterogeneities in transmission geometry: Geophysical Prospecting, **61**, 1238–1251, doi: 10.1111/1365-2478.12065.

Cardarelli, E., M. Cercato, A. Cerreto, and G. Di Filippo, 2010, Electrical resistivity and seismic refraction tomography to detect buried cavities: Geophysical Prospecting, **58**, 685–695, doi: 10.1111/j.1365-2478.2009.00854.x.

Epanomeritakis, I., V. Akçelik, O. Ghattas, and J. Bielak, 2008, A Newton-CG method for large-scale three-dimensional elastic full-waveform seismic inversion: Inverse Problems, **24**, 034015, doi: 10.1088/0266-5611/24/3/034015.

Ernst, J. R., H. Maurer, A. G. Green, and K. Holliger, 2007, Application of a new 2D time-domain full-waveform inversion scheme to crosshole radar data: Geophysics, **72**, no. 5, J53–J64, doi: 10.1190/1.2761848.

Fathi, A., B. Poursartip, K. H. Stokoe, II, and L. F. Kallivokas, 2016, Three-dimensional P- and S-wave velocity profiling of geotechnical sites using full-waveform inversion driven by field data: Soil Dynamics and Earthquake Engineering, **87**, 63–81, doi: 10.1016/j.soildyn.2016.04.010.

Fichtner, A., B. L. Kennett, H. Igel, and H. P. Bunge, 2009, Full seismic waveform tomography for upper-mantle structure in the Australasian region using adjoint methods: Geophysical Journal International, **179**, 1703–1725, doi: 10.1111/j.1365-246X.2009.04368.x.

Grandjean, G., and D. Leparoux, 2004, The potential of seismic methods for detecting cavities and buried objects: Experimentation at a test site: Journal of Applied Geophysics, **56**, 93–106, doi: 10.1016/j.jappgeo.2004.04.004.

Ha, W., S. G. Kang, and C. Shin, 2014, 3D Laplace-domain waveform inversion using a low-frequency time-domain modeling algorithm: Geophysics, **80**, no. 1, R1–R13, doi: 10.1190/geo2013-0332.1.

Komatitsch, D., and R. Martin, 2007, An unsplit convolutional perfectly matched layer improved at grazing incidence for the seismic wave equation: Geophysics, **72**, no. 5, SM155–SM167, doi: 10.1190/1.2757586.

Métivier, L., R. Brossier, Q. Merigot, E. Oudet, and J. Virieux, 2016, An optimal transport approach for seismic tomography: Application to 3D full waveform inversion: Inverse Problems, **32**, 115008, doi: 10.1088/0266-5611/32/11/115008.

Mirzanejad, M., and K. T. Tran, 2019, 3D viscoelastic full waveform inversion of seismic waves for geotechnical site investigation: Soil Dynamics and Earthquake Engineering, **122**, 67–78, doi: 10.1016/j.soildyn.2019.04.005.

Nguyen, T. D., and K. T. Tran, 2018, Site characterization with 3D elastic full-waveform tomography: Geophysics, **83**, no. 5, R389–R400, doi: 10.1190/geo2017-0571.1.

Operto, S., Y. Gholami, V. Prieux, A. Ribodetti, R. Brossier, L. Metivier, and J. Virieux, 2013, A guided tour of multiparameter full-waveform inversion with multicomponent data: From theory to practice: The Leading Edge, **32**, 1040–1054, doi: 10.1190/tle32091040.1.

Pan, W., K. Innanen, G. Margrave, M. Fehler, X. Fang, and J. Li, 2016, Estimation of elastic constants for HTI media using Gauss-Newton and full-Newton multiparameter full-waveform inversion: Geophysics, **81**, no. 5, R275–R291, doi: 10.1190/geo2015-0594.1.

Papadimitriou, D. I., and K. C. Giannakoglou, 2008, Direct, adjoint and mixed approaches for the computation of Hessian in airfoil design problems: International Journal for Numerical Methods in Fluids, **56**, 1929–1943.

Park, C. B., R. D. Miller, and J. Xia, 1999, Multichannel analysis of surface waves: Geophysics, **64**, 800–808, doi: 10.1190/1.1444590.

Plessix, R. É., 2009, Three-dimensional frequency-domain full-waveform inversion with an iterative solver: Geophysics, **74**, no. 6, WCC149–WCC157, doi: 10.1190/1.3211198.

Pratt, R. G., C. Shin, and G. J. Hick, 1998, Gauss–Newton and full Newton methods in frequency–space seismic waveform inversion: Geophysical Journal International, **133**, 341–362, doi: 10.1046/j.1365-246X.1998.00498.x.

Robertsson, J. O., 1996, A numerical free-surface condition for elastic/viscoelastic finite-difference modeling in the presence of topography: Geophysics, **61**, 1921–1934, doi: 10.1190/1.1826736.

Romdhane, A., G. Grandjean, R. Brossier, F. Réjiba, S. Operto, and J. Virieux, 2011, Shallow-structure characterization by 2D elastic full-waveform inversion: Geophysics, **76**, no. 3, R81–R93, doi: 10.1190/1.3569798.

Sheen, D. H., K. Tuncay, C. E. Baag, and P. J. Ortoleva, 2006, Time domain Gauss — Newton seismic waveform inversion in elastic media: Geophysical Journal International, **167**, 1373–1384.

Shen, X., I. Ahmed, A. Brenders, J. Dellinger, J. Etgen, and S. Michell, 2018, Full-waveform inversion: The next leap forward in subsalt imaging: The Leading Edge, **37**, 67b1–67b6, doi: 10.1190/tle37010067b1.1.

Tape, C., Q. Liu, A. Maggi, and J. Tromp, 2010, Seismic tomography of the southern California crust based on spectral-element and adjoint methods: Geophysical Journal International, **180**, 433–462, doi: 10.1111/j.1365-246X.2009.04429.x.

Tran, K. T., and D. R. Hiltunen, 2011, Inversion of first-arrival time using simulated annealing: Journal of Environmental and Engineering Geophysics, **16**, 25–35, doi: 10.2113/JEEG16.1.25.

Tran, K. T., and D. R. Hiltunen, 2012, Inversion of combined surface and borehole first-arrival time: Journal of Geotechnical and Geoenvironmental Engineering, **138**, 272–280.

Tran, K. T., and B. Luke, 2017, Full waveform tomography to resolve desert alluvium: Soil Dynamics and Earthquake Engineering, **99**, 1–8, doi: 10.1016/j.soildyn.2017.04.018.

Tran, K. T., M. McVay, M. Faraone, and D. Horhota, 2013, Sinkhole detection using 2D full seismic waveform tomography: Geophysics, **78**, no. 5, R175–R183, doi: 10.1190/geo2013-0063.1.

Tran, K. T., M. Mirzanejad, M. McVay, and D. Horhota, 2019, 3-D time-domain Gauss–Newton full waveform inversion for near-surface site characterization: Geophysical Journal International, **217**, 206–218, doi: 10.1093/gji/ggz020.

Tran, K. T., and J. Sperry, 2018, Application of 2-D full waveform tomography on land-streamer data for assessment of roadway subsidence: Geophysics, **83**, no. 3, EN1–EN11, doi: 10.1190/geo2016-0550.1.

Vigh, D., J. Kapoor, N. Moldoveanu, and H. Li, 2011, Breakthrough acquisition and technologies for subsalt imaging: Geophysics, **76**, no. 5, WB41–WB51, doi: 10.1190/geo2010-0399.1.

Virieux, J., 1986, P-SV wave propagation in heterogeneous media: Velocity-stress finite-difference method: Geophysics, **51**, 889–901, doi: 10.1190/1.1442147.

Vireux, J., and S. Operto, 2009, An overview of full-waveform inversion in exploration geophysics: Geophysics, **74**, no. 6, WCC1–WCC26, doi: 10.1190/1.3238367.

Warner, M., A. Ratcliffe, T. Nangoo, J. Morgan, A. Umpleby, N. Shah, V. Vinje, I. Štekl, L. Guasch, C. Win, and G. Conroy, 2013, Anisotropic 3D full-waveform inversion: Geophysics, **78**, no. 2, R59–R80, doi: 10.1190/geo2012-0338.1.